# IX-I Development of New Nanomaterials as Components in Advanced Molecular Systems

Nanometer-sized materials exhibit unique electronic behavior. In the quest of advanced redox catalysis, we are currently interested in combining nanometer-sized materials into molecular redox systems. As a basic architecture, composites of organic molecules and gold nanoparticles were synthesized and molecular dynamic simulations were carried out to predict the solution structures.

## IX-I-1 Gold Nanoparticles Stabilized by Tripod Thioether Oligomers: Synthesis and Molecular Dynamics Studies

**HOSOKAWA, Youichi; MAKI, Suguru; NAGATA, Toshi**

[*Bull. Chem. Soc. Jpn.* in press (2005)]

Gold nanoparticles (1.5–1.7 nm) were prepared by use of three tripod thioether oligomers (TTOs) as stabilizing molecules shown in Figure 1. The ICP-AES analyses of these TTO/$Au_n$ composites revealed the number of protecting molecules per nanoparticles as 25±19, 23±21, and 10±6. On the other hand, the molecular models suggested that the TTOs were of comparable sizes with the sizes of nanoparticles. In order to account for this discrepancy, we carried out molecular dynamic simulations of the TTO/$Au_n$ composites. The interaction parameters between organic molecules and the gold surface were newly developed so that they reproduced the adsorption enthalpies of small sulfur-containing molecules on the Au(111) surface. By use of these parameters, the self-assembly process of TTO molecules on the $Au_{147}$ surface was simulated in chloroform solvent. Figure 2 shows the typical results from a single run, in which 16 TTO molecules (**1a**) and an $Au_{147}$ nanoparticle (a cuboctahedral structure; diameter 1.7 nm) were placed in a box of $CHCl_3$ with dimensions 112.2×96.3×97.7 $Å^3$. The surface of the gold nanoparticle was completely covered with three TTO molecules. Although it is not impossible to accommodate more than 20 **1a**'s around the surface of a gold nanoparticle, the more appropriate model would be coexistence of free, unbound **1a** molecules and gold nanoparticles covered with a small number of **1a**. The free and bound **1a** molecules should be in dynamic equilibrium in $CHCl_3$ solutions, as suggested by the $^1H$ NMR spectra which showed only one set of slightly broadened signals.

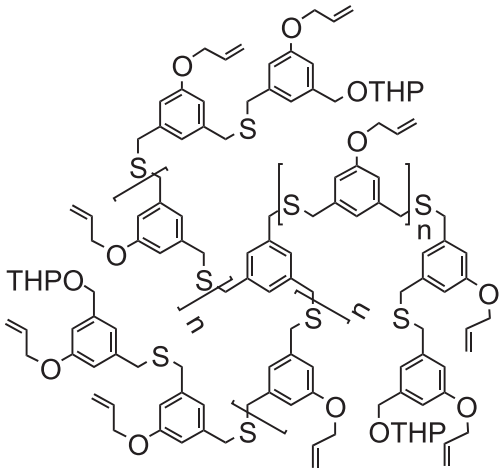


**1a**: n = 1, **1b**: n = 3, **1c**: n = 5

**Figure 1.** The tripod thioether oligomers used in this study.

**Figure 2.** A snapshot structure from the **1a**$_{16}$/$Au_{147}$ simulation, in which three **1a** molecules are adsorbed on the $Au_{147}$ surface. The space-filling views from two opposite directions are shown. The gold nanoparticle and the three different **1a** molecules are denoted in white color and three different levels of gray colors, respectively.

# IX-J Designing Artificial Photosynthesis at Molecular Dimensions

Photosynthesis is one of the finest piece of molecular machinery that Nature has ever created. Its ultrafast electron transfer and following well-organized sequence of chemical transformation have been, and will continue to be, challenging goals for molecular scientists. Our ultimate goal is to design artificial molecular systems that effect multiple chemical reactions triggered by light on the basis of molecular rationale.

### IX-J-1 Electrochemical Properties of Ferrocene-Dendrimer-Porphyrins

**KIKUZAWA, Yoshihiro; NAGATA, Toshi**

Synthesis of the ferrocene-dendrimer-porphyrins (Figure 1) was already reported in previous Annual Reviews. Figure 2 shows the differential pulse voltammograms (DPV) of **G*n*(Fc)$_m$-ZnP**, together with the reference compounds **Bn-ZnP** and **Fc-ZnP**, in $CH_2Cl_2$/0.1 mol/dm$^3$ $Bu_4NClO_4$. The ferrocene-dendrimer-porphyrin compounds showed three oxidation peaks at 0.2, 0.5 and 0.7 V (*vs* $FeCp_2/FeCp_2^+$), which were assigned as the oxidation of the ferrocenyl groups, and the first and second oxidation of the porphyrin. Figure 3 shows the plots of $i_{max}$ (the peak height) versus $\Delta t^{-1/2}$ ($\Delta t$ is the pulse width) for the first two oxidation peaks of **G3(Fc)$_{14}$-ZnP**. The values for peak II showed good linearity, whereas those for peak I showed pronounced deviation from linearity. These results indicate that the electron transfer for the first oxidation (peak I) is slow in the electrochemical timescale. This slow kinetics can be attributed to the reorganization of the supporting electrolyte during the multiple electron transfer of the ferrocene-dendrimer redox pool.

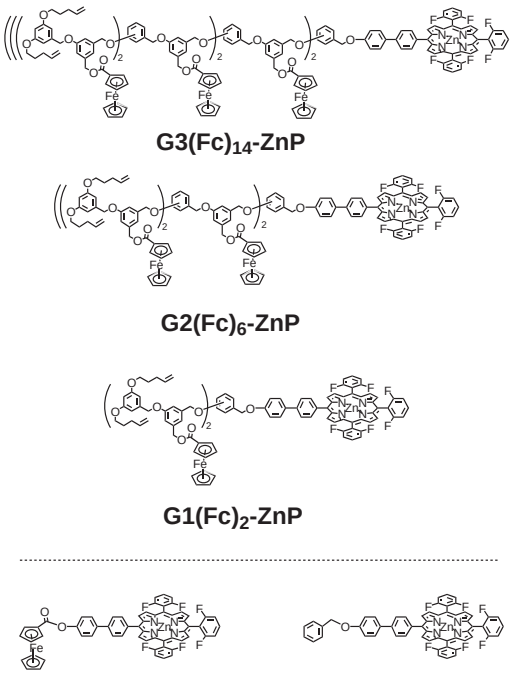


**Figure 1.** The structure of the ferrocene-dendrimer-linked porphyrins.

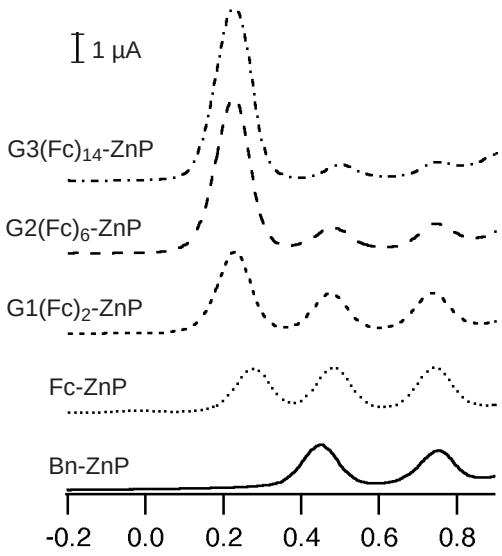


**Figure 2.** The differential pulse voltammograms of the ferrocene-dendrimer-porphyrins.

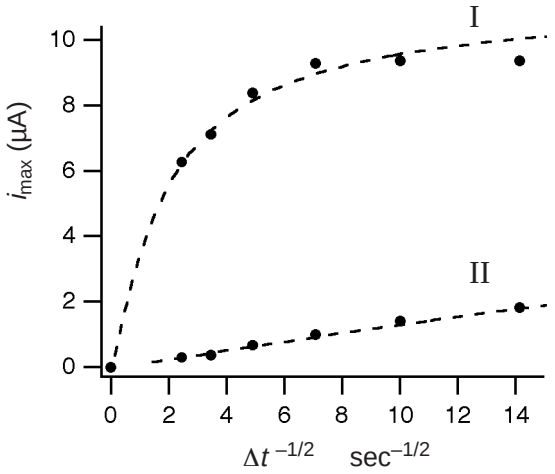


**Figure 3.** The $i_{max}$-$\Delta t^{-1/2}$ plots of the first two oxidation peaks of **G3(Fc)$_{14}$-ZnP**.

# IX-K Development of New Metal Complexes as Redox Catalysts

Redox catalysis is an important field of chemistry which translates a flow of electron into chemical transformation. It is also one of the requisites for artificial photosynthesis. This project of ours aims at developing new metal complexes that perform redox catalysis at low overpotential. Currently we are focusing our attention to the development of a series of cobalt phosphine complexes as possible catalysts for electrochemical reductions.

## IX-K-1 Synthesis, Structure and Electrochemistry of New Cobalt Complexes with Cyclopentadienyl and Bidentate Ligands

**NAGASAWA, Takayuki; NAGATA, Toshi**

Low-valent cobalt complexes are interesting candidates for electrocatalytic reductions. Herein we report the synthesis, structure, and electrochemistry a series of cobalt complexes with general formula $[Cp^*Co(L)(S)]^{2+}$, where Cp* is pentamethylcyclopentadienyl anion, L is a bidentate ligand and S is an exchangable monodentate ligand.

The key intermediate compound, $[Cp^*Co(SMe_2)_3](BF_4)_2$, was prepared from $Cp^*Co(CO)_2$ by a similar method as the Cp analog reported by Kuhn. The reaction of this compound with a bidentate ligand in $CH_3NO_2$, followed by treatment with $CH_3CN/Et_2O$, gave a crystalline product $[Cp^*Co(L)(CH_3CN)](BF_4)$ in 80–90% yield (Scheme 1). The X-ray structure of **2** (L = dppp) is shown in Figure 1, which shows typical octahedral coordination of the Co(III) center. The cyclic voltammograms in $CH_3CN$ showed two reversible waves corresponding to the Co(III)/Co(II) and Co(II)/Co(I) redox couples (Table 1).

$[Cp^*Co(SMe_2)_3](BF_4)_2$ + L

↓ 1. $MeNO_2$, r.t. 2. $CH_3CN/Et_2O$

$[(Cp^*Co(L)(CH_3CN)](BF_4)_2$

L = $Ph_2P(CH_2)_2PPh_2$ (**1**)
$Ph_2P(CH_2)_3PPh_2$ (**2**)
2,2'-bipyridyl (**3**)
$H_2N(CH_2)_2NH_2$ (**4**)

**Scheme 1.** Synthesis of the cobalt complexes.

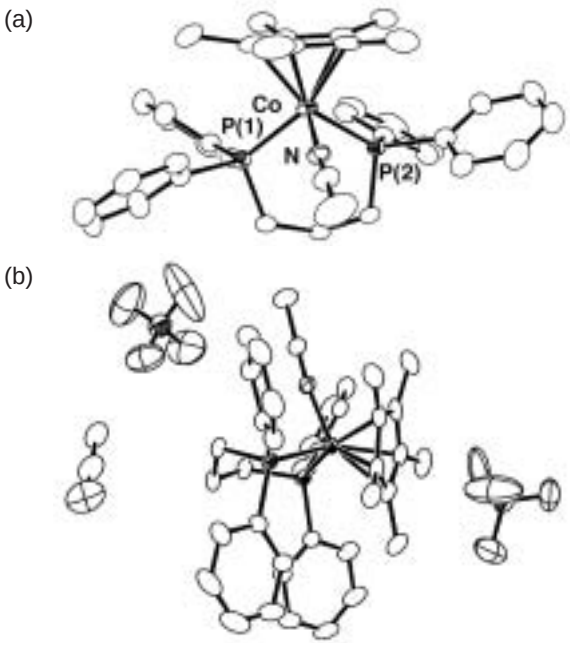


**Figure 1.** The ORTEP drawings of (a) the cationic part, and (b) the asymmetric unit of **2**.

**Table 1.** The reversible half-wave potentials of **1**-**4** in $CH_3CN/Bu_4NClO_4$.

| | $E_{1/2}$(V vs. $Cp_2Fe/Cp_2Fe^+$) Co(III)/Co(II) | Co(II)/Co(I) |
|---|---|---|
| **1** | **-0.61** | **-1.13** |
| **2** | **-0.56** | **-1.26** |
| **3** | **-0.82** | **-1.15** |
| **4** | **-0.98** | **-2.25** |